JACS
JOURNAL OF THE AMERICAN CHEMICAL SOCIETY

Article

pubs.acs.org/JACS

Anisotropic MRI Contrast Reveals Enhanced Ionic Transport in Plastic Crystals

Konstantin Romanenko,*[,†] Liyu Jin,[‡,§] Louis A. Madsen,[∥] Jennifer M. Pringle,[†,‡] Luke A. O'Dell,[†] and Maria Forsyth*[,†,‡]

[†]Institute for Frontier Materials, Deakin University, Waurn Ponds Campus, 75 Pigdons Road, Geelong, Victoria 3220, Australia

[‡]ARC Centre of Excellence for Electromaterials Science, Deakin University, Burwood Campus, 221 Burwood Highway, Burwood, Victoria 3125, Australia

[§]Department of Materials Engineering, Monash University, Wellington Road, Clayton, Victoria 3800, Australia

[∥]Department of Chemistry and Macromolecules and Interfaces Institute, Virginia Tech, Blacksburg, Virginia 24061, United States

Supporting Information

ABSTRACT: Organic ionic plastic crystals (OIPCs) are attractive as solid-state electrolytes for electrochemical devices such as lithium-ion batteries and solar and fuel cells. OIPCs offer high ionic conductivity, nonflammability, and versatility of molecular design. Nevertheless, intrinsic ion transport behavior of OIPCs is not fully understood, and their measured properties depend heavily on thermal history. Solid-state magnetic resonance imaging experiments reveal a striking image contrast anisotropy sensitive to the orientation of grain boundaries in polycrystalline OIPCs. Probing triethyl(methyl)phosphonium bis(fluorosulfonyl)imide ($P_{1222}FSI$) samples with different thermal history demonstrates vast variations in microcrystallite alignment. Upon slow cooling from the melt, microcrystallites exhibit a preferred orientation throughout the entire sample, leading to an order of magnitude increase in conductivity as probed using impedance spectroscopy. This investigation describes both a new conceptual window and a new characterization method for understanding polycrystalline domain structure and transport in plastic crystals and other solid-state conductors.

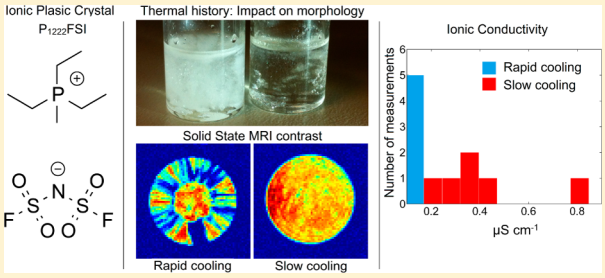

1. INTRODUCTION

Organic ionic plastic crystals (OIPCs) are purely ionic solids in which the charged molecules are located on ordered sites in a periodic lattice and also show local orientational and dynamic disorder. OIPCs demonstrate unique combinations of properties, such as nonflammability, low volatility, plasticity, high electrochemical and thermal stability, and most importantly high ionic conductivity (up to 10^{-2} S cm^{-1} at 25 °C).[1] These features make OIPCs extremely attractive candidates for electrolytes in electrochemical devices including lithium-ion batteries and solar and fuel cells.[2−7] However, the ion transport properties of different OIPCs, and in different phases of a particular OIPC, can vary dramatically.[8−10] Given the vast variety of cation and anion combinations available, an improved fundamental understanding of transport mechanisms and temperature-dependent phase behavior will be crucial for the rational design of improved OIPC-based electrolytes.[11]

The phosphonium-based OIPC triethyl(methyl)-phosphonium bis(fluorosulfonyl)imide ($P_{1222}FSI$, Figure 1a) has been shown to exhibit significant intrinsic ionic conductivity in the solid state at room temperature.[8] Thermal analysis of this OIPC shows a sharp melting point at 47 °C as well as a main solid−solid phase transition at −55 °C (Figure 1b). In the intermediate range of temperatures (Phase I), $P_{1222}FSI$ shows a temperature-dependent conductivity ranging from 10^{-8} to 10^{-6} S cm^{-1}.

After melting and subsequent cooling to room temperature, the visual appearance of solid-phase $P_{1222}FSI$ is found to vary depending on the cooling rate. Figure 1c shows two $P_{1222}FSI$ samples cooled from the melt under distinctly different conditions: (left) rapid cooling (quenching) from the melt by immersion of the container in a 6 °C water bath, with apparent solidification occurring after 1 min, and (right) slow, controlled cooling to room temperature (21 °C) over a period of 48 h. In Figure 1c, the quenched $P_{1222}FSI$ sample is opaque-white in appearance (left), while the slowly cooled sample is clear and colorless (right).

The ability to monitor polycrystalline texture, polymorphic phase composition and transitions in OIPCs *in situ* and with spatial resolution has significant practical value. Conventional electron microscopy (SEM and TEM) studies of polymers and OIPCs face problems such as sensitivity of the sample to electron beam irradiation, sample preparation, difficult data interpretation due to low contrast between structural details, and the inability to probe interior 3D morphology.[12] Here, we

Received: August 12, 2014
Published: October 14, 2014

   dx.doi.org/10.1021/ja508290z | J. Am. Chem. Soc. 2014, 136, 15638−15645

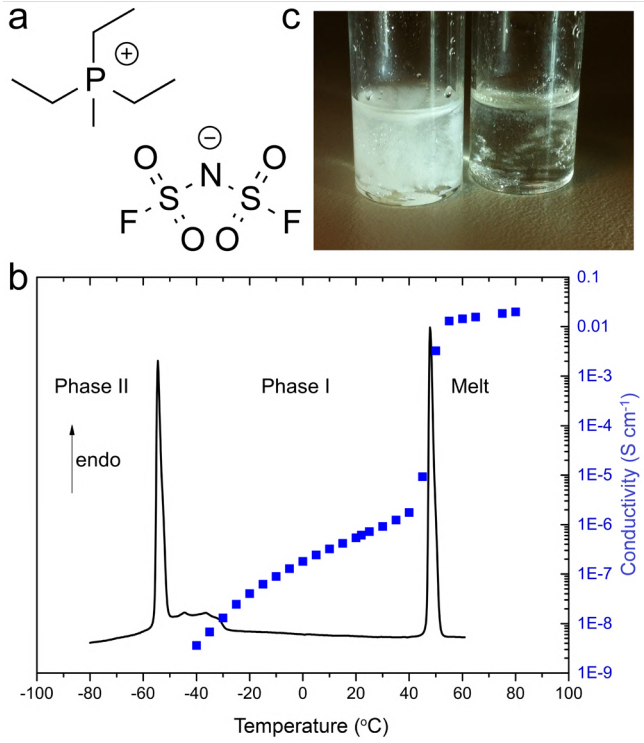

Figure 1. Properties of $P_{1222}FSI$. (a) Chemical structure. (b) Differential scanning calorimetry trace of $P_{1222}FSI$, superimposed on the ionic conductivity measured by AC impedance spectroscopy. (c) Photograph of two $P_{1222}FSI$ samples cooled from the melt in 1 min (left) and over 48 h (right).

have employed magnetic resonance imaging (MRI) experiments to study the effects of thermal history on morphological and transport properties of OIPCs.

NMR spectroscopy and MRI are nondestructive methods offering a highly versatile approach for the *in situ* characterization of spatially dependent structure and dynamics in solid materials. These techniques have recently attracted interest in the *in situ* study of batteries and fuel cells.[13−18] The pulsed-field-gradient (PFG) principles[19,20] allow MRI experiments to be specifically tailored to study various physical, chemical, or biological phenomena and offer a range of options for generating image contrast. The relaxation time constants T_1, T_2, and T_2*[19] associated with the nuclear magnetization are of primary importance in determining the MRI technique that is optimal in terms of sensitivity, resolution, and time efficiency. The transverse relaxation time constant, T_2*, defines the rate at which the measured MR free induction decay (FID) occurs:

$$1/T_2^* = 1/T_2 + \gamma \Delta B_0/2\pi \quad (1)$$

where γ is the nuclear gyromagnetic ratio. The decay rate is driven by dynamic processes (the $1/T_2$ term) as well as by μm to mm scale spatial variations in the magnetic field (ΔB_0) that can arise from internal material morphological features[21−24] or even from intentional T_2* manipulation.[25]

Solids such as OIPCs can exhibit ^{1}H T_2* values as short as a few μs, corresponding to NMR spectral line widths approaching 50 kHz.[9] MRI of such systems can be successfully achieved using single point imaging (SPI) methods,[26,27] which do not employ spin or gradient echoes and involve only phase encoding principles.[19] We have therefore used single point ramped imaging with T_1 enhancement (SPRITE),[27,28] a time-efficient, SPI method that allows quantitative, distortion free imaging of materials with short transverse relaxation times. SPRITE has previously been used in studies of sedimentary materials,[24,29] polymers,[30] prostheses,[31] and bones.[32] Several other MRI methods[33−36] are also notable for their utility in solid materials imaging.

2. EXPERIMENTAL DETAILS

2.1. Sample Preparation. $P_{1222}FSI$, $P_{1444}FSI$, and $P_{1224}PF_6$ were prepared as described elsewhere.[8] For MRI experiments OIPC samples were packed into 25 and 16 mm outer diameter (o.d.) glass vials. Quenching protocols: The vials were heated to 100 °C, and after complete OIPC melting were immersed into reservoirs with either liquid N_2 (77 K), chilled H_2O (279 K), or at ambient temperature (293 K). Slow cooling protocol: The vial containing the melted OIPC was placed in an aluminum vessel preheated to 100 °C. The vessel was cooled to 21 °C over 48 h with a temperature-controlled hot plate and avoiding sample vibration. Samples were equilibrated at 21 °C for 24 h.

2.2. Magnetic Resonance Imaging. Experiments were performed on a Bruker Avance−III system equipped with a 11.75 T vertical 89 mm bore magnet (500.07 MHz ^{1}H frequency). A water-cooled Micro2.5 gradient set driven by three GREAT (1/60) amplifiers provided gradient strengths up to 1.5 T m^{-1}. A MICWB40 radio frequency (RF) probe with a 25 mm diameter quadrature birdcage resonator was used for ^{1}H MRI and static ^{1}H NMR. The SPRITE pulse sequences were developed under the Bruker Paravison environment. The 3D *k*-space sampling strategy employed eight centrically ordered sectoral interleaves covering a square region of *k*-space 65 × 65 in the transverse (k_x−k_y) plane. In the third dimension (Z) the gradient was incremented linearly in 65 steps. The SPRITE sequence parameters were: maximum amplitude of the imaging gradient, 0.4 T m^{-1}; RF pulse repetition time (T_R), 1.3 ms; RF pulse duration, 2 μs ($\alpha \approx \pi/40$); minimum phase encoding time (T_P) 67 μs; magnetization recovery delay, 4 s; number of signal averages, 1; and image acquisition time, 40 min. The diffusion tensor was calculated from apparent diffusion coefficients measured along six noncollinear directions at 18 °C. Cotts PFG diffusometry measurements employed a bipolar gradient scheme (13 interval, condition I)[37] and a four-step phase cycle.[38] The parameters of the PFG diffusometry experiments were: maximum g_a, 1.4 T m^{-1}; effective gradient duration (δ) 1−2 ms; STE intervals (τ) 4.5−6 ms; observation z-storage interval (Δ) 10−300 ms; NA, 4; excitation and refocusing pulse durations were 35 and 70 μs, respectively. The sample temperature during the measurements was 18 °C. The MRI data were processed using Matlab (R2013a, The MathWorks, Inc.).

2.3. Conductivity Measurements. Ionic conductivity was measured by AC electrochemical impedance spectroscopy (EIS) with an HP4284A impedance meter. A homemade conductance cell with two platinum blocking electrodes was employed, and the cell constants were calibrated with a 0.01 M KCl solution. The OIPC sample was packed in a nitrogen atmosphere and kept hermetically sealed throughout the measurements. Prior to each measurement, the sample was premelted at 90 °C in the conductance cell, which as a whole was heated in a muffle furnace to remove any possible thermal history before proceeding to different heat treatments. The slow cooling was performed on the cell at a controlled rate of 0.1 °C min^{-1} in the muffle furnace, while quenching was achieved at a rate of about 90 °C min^{-1} with a −20 °C PID controlled brass block. In both cases, the sample was then equilibrated at 25 °C for 12 h before conductivity measurements. The sample was cooled from the melt with electrodes already in position to ensure good contact at the interfaces. This prevented alterations of the sample microstructures and mechanical disruptions that would occur as a result of insertion of the electrodes. EIS data were collected over a frequency range from 10 MHz to 20 Hz using a signal amplitude of 0.1 V at 25 °C. The cell temperature was controlled by a Eurotherm-2204, within 0.1 °C tolerance.

dx.doi.org/10.1021/ja508290z | J. Am. Chem. Soc. 2014, 136, 15638−15645

3. RESULTS AND DISCUSSION

3.1. SPRITE Imaging. In the SPRITE MRI method the imaging gradients are incremented in a stepwise manner with a millisecond period, T_R. Each gradient increment is followed by a gradient stabilization time, a hard (RF) pulse, phase encoding time (T_P), and signal acquisition. Only one point of the FID signal per gradient step is enough to reconstruct the image. The RF pulse should be short enough to excite the maximum sample bandwidth, $w = \gamma GL/2\pi$, where G is the maximum gradient magnitude, and L is the sample dimension along the gradient direction. The use of low flip angle RF pulses ($\alpha \ll \pi/2$) and interleaved k-space sampling substantially reduces the extent of image blurring resulting from longitudinal magnetization saturation effects.[28] The sensitivity and resolution limitations stem also from the MRI hardware performance. Limited gradient strength and finite RF probe "dead time" dictate the minimum T_P to be a few tens of microseconds. Thus, NMR signals ≈30 kHz wide can be observed in SPRITE. Centric ordering of the k-space trajectories is a key-factor for the quantitative image accuracy. The centric scan SPRITE[28] image intensity, $I(r)$, as a function of position r is described by

$$I(r) = \rho(r)\cdot\exp(-T_P/T_2^*)\sin(\alpha) \quad (2)$$

Here, $\rho(r)$ is the nuclear spin density, T_P is the MR phase encoding time during which signal decay occurs, and α is the flip angle of the RF excitation pulses. Since α is constant over the sample, SPRITE can take advantage of two potential sources of image contrast: ρ and T_2^*. T_2^* is sensitive to both magnetization dephasing due to magnetic field gradients and dipolar couplings which characterize the local crystal structure.

The transverse relaxation rate $(T_2^*)^{-1}$, i.e., the ^{1}H NMR line width, measured in $P_{1222}FSI$, was found to increase with the magnetic field strength B_0. This is commonly observed in multiphase systems where spatial variation of magnetic susceptibility causes internal magnetic field gradients, g_i. For example, this magnetic susceptibility contrast is a main source of B_0-dependent T_2^* in porous media such as sedimentary rocks and granular systems.[21−24] In this study the sensitivity of the SPRITE image contrast, eq 2, to internal gradients and dipolar couplings reveals phenomena related to the polycrystalline nature of the OIPC and the presence of amorphous intercrystalline domains with a high intrinsic mobility through which the ion transport occurs.

3.2. Anisotropic T_2^* contrast in $P_{1222}FSI$. Figure 2a shows slices through a 3D ^{1}H SPRITE image taken from a sample of $P_{1222}FSI$ rapidly cooled from the melt. Sharp intensity contrast (>10:1) arises from mm-scale domains that differ significantly in T_2^*. This assumption was confirmed using variable T_P experiments (Supporting Information, Figure S1) showing a surprisingly broad range of T_2^* values (10−70 μs). Distinct domain morphologies can be observed, including a conical feature extending upward from the bottom of the 25 mm o.d. vial and needle-like regions extending radially inward from the container walls. This morphology suggests that domains grew inward from nucleation sites located on the inside surface of the vial during quenching. As the plastic crystal undergoes homogenization while in the molten state, the exact domain morphologies that occur upon solidification are never reproduced, and repetitive melting and quenching cycles result in similar but not identical MRI intensity contrast patterns. Figure 2b shows SPRITE images of a $P_{1222}FSI$ sample cooled slowly from above the melt temperature over a period of 48 h.

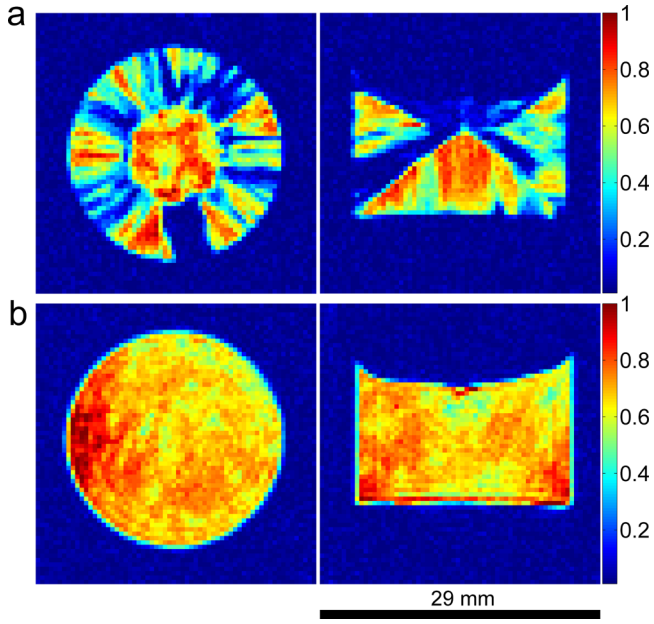

Figure 2. Effects of thermal history on polycrystalline morphology of $P_{1222}FSI$. (a) Transverse (left) and longitudinal (right) slices through a 3D ^{1}H SPRITE image of $P_{1222}FSI$ after rapid (1 min) cooling from the melt in a 25 mm o.d. vial. (b) Transverse (left) and longitudinal (right) slices through a 3D ^{1}H SPRITE image of $P_{1222}FSI$ after slow (over 48 h) cooling from the melt in a 25 mm o.d. vial (T_P, 107 μs; resolution, 0.44 mm; T = 18 °C).

In this case the image shows an entirely different domain morphology, indicating a rather uniform T_2^* distribution over the sample volume.

The individual domains in these images do not arise from macroscopic single crystals as one might first assume, and an additional phenomenon observed in these experiments can help to explain why. Upon rotation of the samples about the direction of the externally applied magnetic field B_0, the T_2^* contrast and image intensity change significantly. Figure 3 illustrates this for a rapidly cooled sample (images are shown in the sample reference frame for convenience of the eye, while the arrows indicate the direction of B_0). Distinct domain layouts can be seen at eight different orientations in Figure 3. Some of the largest domains (∼10 mm) preserve their shape while changing intensity, and other domains split into several subdomains. Since T_2^* is a reflection of ^{1}H NMR line width, the ^{1}H spectrum arising from a particular domain depends on the sample orientation. We believe this represents the first observation of such MRI contrast anisotropy in a pure polycrystalline material, thus opening new avenues to understanding novel domain structure in a range of solids.

Figure 4a shows the SPRITE images obtained from a slowly cooled sample at four different orientations (this time B_0 points vertically upward in all cases), and Figure 4b shows the dependence of the integrated (average) image intensities on the polar angle in the range from 0 to 2π. A strong orientation dependence of the ^{1}H NMR line width (Supporting Information, Figure S2) is consistent with the T_2^*-weighted SPRITE image intensity as described by eq 2.

Note that the period of intensity variation with angle depends on the axis of sample rotation. At 11.75 T the lineshapes of the ^{1}H NMR spectra are composed of both wide (10−50 kHz) and narrow (0.5−1.5 kHz) components. The narrow component is strong evidence for highly dynamic P_{1222}

dx.doi.org/10.1021/ja508290z | J. Am. Chem. Soc. 2014, 136, 15638−15645

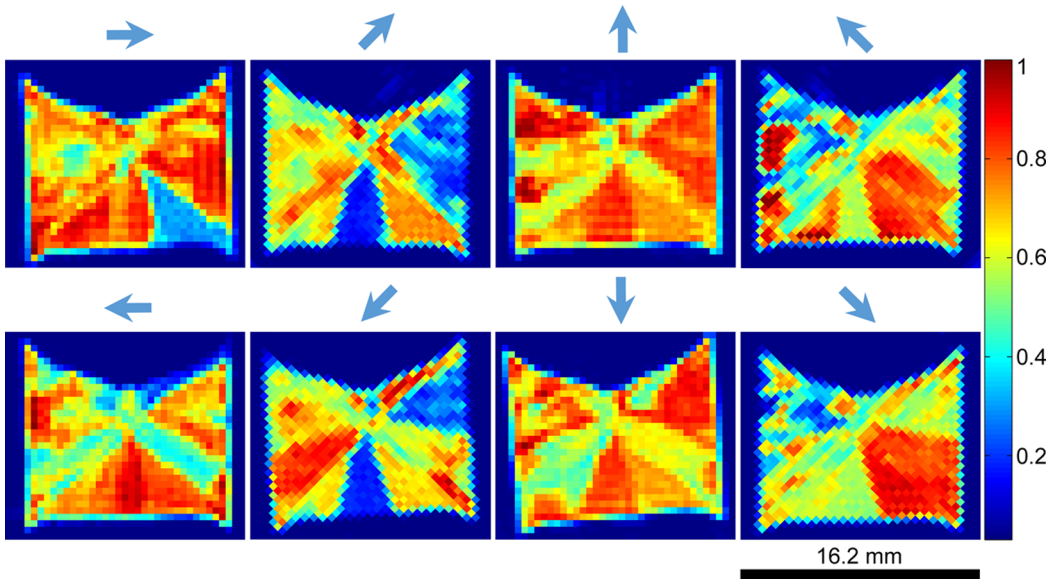

Figure 3. Orientation dependence of the ^{1}H SPRITE T_2* contrast in the rapidly cooled P_{1222}FSI. Representative longitudinal slices through 3D ^{1}H SPRITE images of the rapidly cooled P_{1222}FSI sample set at different orientations within the magnet (T_P = 67 μs; resolution, 0.44 mm; T = 18 °C). Selected slices are perpendicular to the axis of rotation and shown at a fixed location on this axis. The acquired images were subsequently rotated to align them in the sample frame (the blue arrow above each image shows the direction of B_0). 3D images were scaled by a common maximum intensity value.

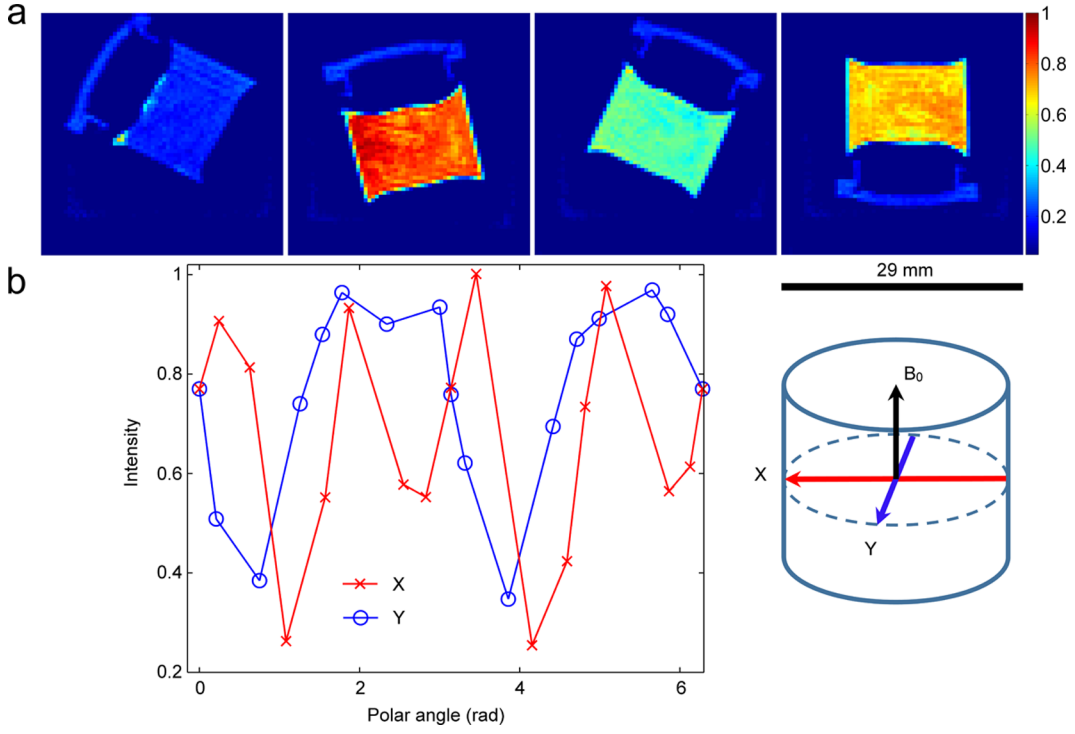

Figure 4. Orientation dependence of the ^{1}H SPRITE T_2* contrast in the slowly cooled P_{1222}FSI. (a) Representative longitudinal slices through 3D ^{1}H SPRITE images of the slowly cooled P_{1222}FSI sample set at different orientations within the magnet. Selected longitudinal slices (laboratory reference frame) are perpendicular to the axis of rotation and shown at a fixed location on this axis. The plastic cap sealing the sample vial is also visible in these images and serves as an internal reference for the signal intensity (T_P = 67 μs; resolution, 0.44 mm; T = 18 °C). (b) Average SPRITE intensity as a function of polar angle resulting from rotation about two perpendicular axes X and Y in the transverse plane (as indicated on the right). Local image intensities and the average intensity vary coherently.

molecules within the solid sample, existing as an amorphous mobile phase that constitutes approximately 2% of the total sample at room temperature.

The origin of this orientation dependent T_2* can be understood by modeling the OIPC as a polycrystalline system with a finite mobile layer between the microcrystallites (Figure 5). This "liquid-like" grain boundary phase will exhibit a different magnetic susceptibility to the crystalline phase. According to established theory describing magnetic field vector boundary conditions[39] a magnetic field gradient will arise

dx.doi.org/10.1021/ja508290z | J. Am. Chem. Soc. 2014, 136, 15638−15645

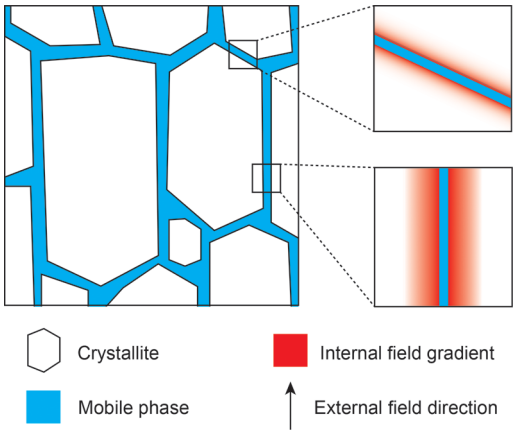

Figure 5. Schematic illustrating the nature of SPRITE T_2* contrast anisotropy. The magnitude and extent of the local magnetic field gradient arising at the interface between two phases with different magnetic susceptibilities (in this case solid crystals and a mobile amorphous component) depends on the orientation of that interface with respect to the external field, B_0.

across the interface between the two phases in the presence of an external magnetic field B_0. The gradient magnitude, g_i, depends on orientation of the interface with respect to B_0 and also scales linearly with B_0. T_2* will therefore be sensitive to local magnetic field inhomogeneity (ΔB_0) proportional to g_i, eq 1.

Another potential source of the orientation-dependent T_2* is related to dipolar couplings between protons, an interaction proportional to $3\cos^2(\theta) - 1$, where θ is the angle between the interspin vector and B_0. A significant dipolar NMR broadening (≈10 kHz) can be observed in OIPCs.[9] Although the distribution of ^{1}H−^{1}H vectors in P_{1222}FSI system appears to be macroscopically isotropic, residual orientation dependence should also be expected. The orientation-dependent SPRITE intensities (Figures 3 and 4) therefore constitute evidence for anisotropy in the distribution of crystallite orientations. Note that since g_i effectively decays over μm scale distances from the interface,[21,22] macroscopic crystallites (100 μm scale or larger) would show negligible orientation dependence of the second term in eq 1.

Each macroscopic domain with uniform T_2* in Figures 2−4 thus represents a region composed of crystallites exhibiting some form of preferred orientation. The actual orientation within each domain likely depends on the orientation of the very first crystallite formed at the nucleation site during the cooling process. During rapid cooling, many nucleation sites occur, and multiple domains form. Conversely, during slow cooling, the first nucleation site has time to grow over the full sample volume and can result in a single domain. Note that disorder in microcrystallite orientations on length scales significantly smaller than the MRI voxel size would lead to no observable MRI intensity orientation dependence.

Figure 4b shows how the SPRITE image intensity (average over the sample region) passes through reproducible minima and maxima associated with the directions of preferential grain boundary orientation. The boundaries aligned with B_0 create the strongest g_i (shortest T_2*) and thus the lowest image intensity. It should also be noted that the periodic dependence of the image intensity (Figure 4b) will be determined by the crystallite shape and symmetry.

3.3. NMR Diffusometry and Internal Gradients. PFG NMR diffusometry[20] experiments allow for the direct measurement of ion transport in OIPCs. The conventional Tanner stimulated echo (STE) technique[40] is prone to substantial errors due to superposition of the applied (g_a) and internal (g_i) magnetic field gradients. A more advanced pulse sequence by Cotts[37] utilizes bipolar gradient pulses to eliminate the g_a g_i superposition effects, thus providing an accurate apparent diffusion coefficient (D_a). As a result, the difference in D_a's obtained by the two methods can be used to estimate the effective internal gradient strength g_i. STE signal attenuations measured by Tanner and Cotts methods are described by functions f_T and f_C, respectively:[3]

$$f_T = \ln(I_T/I_0) = -D_{aT}A(g_a\ g_i) \tag{3}$$

$$f_C = \ln(I_C/I_0) = -D_{aC}B(g_a) \tag{4}$$

where D_{aT} and D_{aC} are diffusivities obtained by the Tanner and Cotts methods, respectively:

$$A(g_a g_i) = \gamma^2\delta^2 g_a^2(\Delta + \tau - \delta/3) + \gamma^2\delta(2\tau\Delta + 2\tau^2 - 2\delta^2/3 - 2\delta\delta_1 - 2\delta_1^2)g_a g_i$$

and

$$B(g_a) = 4\gamma^2 g_a^2\delta^2(\Delta + 1.5\tau - \delta/6)$$

The intervals τ, Δ, δ, and δ_1 of the STE pulse sequences are described elsewhere.[37] Expressions 3 and 4 allow calculation of the diffusivity values from the dependence of echo attenuation on the applied gradient g_a.

The broad NMR signals coming from the solid phase of P_{1222}FSI vanish during the PFG-STE encoding intervals (τ), and only narrow (≈1 kHz) signals are observed. The Cotts method resulted in a highly linear Stejskal−Tanner signal decays for observation intervals, Δ, in a range from 14 to 100 ms. The Tanner method showed concave-shaped echo attenuation suggesting the presence of considerable internal field gradients. This is supported by the fact that when $g_a \gg g_i$ the slope of the Tanner plot should asymptotically approach the slope of the Cotts plot describing the accurate diffusivity value. The experimental plot f_T vs $A(g_a g_i)$ is noticeably concave when $g_i = 0$ (Figure 6). It gradually straightens at increasing g_i and approaches the Cotts decay. Assuming that D_{aC} is an accurate diffusivity value, condition $D_{aT} = D_{aC}$ gives $\langle g_i \rangle \approx 0.19$ T m^{-1}. This value corresponds to an effective internal gradient as sampled by molecules at a short-range displacement ≈1 μm. We also observed that $<g_i>$ decreases gradually with increasing PFG observation time (Δ) due to averaging over an increasing grain boundary space.

The narrow ^{1}H NMR signal arising from the mobile phase (line width $\Delta\nu \approx 500$ Hz) can only be observed in the presence of magnetic field gradient g_i if $L < 2\pi\ \Delta\nu/\gamma\ g_i \approx 6$ μm, where L is a length scale associated with the width of the intercrystallite mobile layer and γ is the ^{1}H gyromagnetic ratio. Further analysis shows that the mobile phase diffusion is restricted within compartments <1 μm wide. Moreover, the optical translucency of the slow cooled P_{1222}FSI (Figure1c, right) indicates that scattering defects do not exceed the optical light wavelength (~500 nm). Earlier reported SEM images of other OIPCs indicated the presence of grain boundaries a few hundreds of nm wide.[41,42]

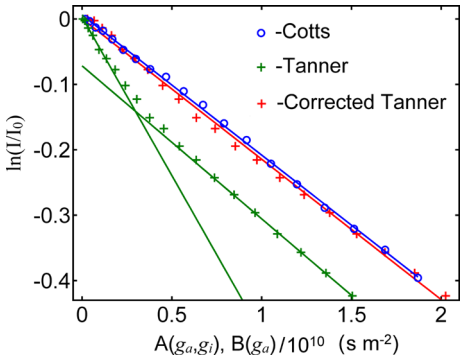

Figure 6. PFG NMR diffusion measurements in $P_{1222}FSI$. A comparison of STE attenuation data obtained with Tanner and Cotts methods (Δ = 10 ms) in a slowly cooled $P_{1222}FSI$. Linear fitting of the Cotts data provides an accurate diffusivity value (D_{aC} = 2.15 × 10^{-11} m^2 s^{-1}). The slopes of the Tanner attenuation curve evaluated at its initial and ending parts are 4.9 and 2.4 × 10^{-11} m^2 s^{-1}, respectively. The corrected Tanner plot obtained with $\langle g_i \rangle$ = 0.19 T m^{-1} gives $D_{aT} = D_{aC}$.

A slight decrease (10−30%) in D_{aC} with Δ indicates restricted diffusion.[3] The sensitivity of the PFG NMR method is limited by the shortest observation interval ≈14 ms, which gives an estimate of the upper limit for the compartment width $L \approx 0.7$ μm at D_{aC} = 2.15 × 10^{-11} m^2 s^{-1}. The extent of diffusion anisotropy is commonly quantified by a fractional anisotropy parameter:

$$\mathrm{FRA} = (((L_1 - L_2)^2 + (L_2 - L_3)^2 + (L_1 - L_3)^2) / 2(L_1^2 + L_2^2 + L_3^2))^{1/2} \quad (5)$$

where L_i are the diffusion tensor eigen values. The diffusion tensor measurements performed in a slowly cooled $P_{1222}FSI$ by Cotts and Tanner methods showed FRA values of 5 and 30%, respectively. Noticeable FRA values obtained by the Tanner method may indicate a macroscopic anisotropy of internal magnetic field gradients.

A systematic variation in the measured diffusion coefficient was observed as a function of cooling rate. Cooling with liquid N_2, or in a chilled H_2O jacket (6 °C), or in ambient air (21 °C), or with a temperature-controlled hot plate resulted in D_{aC} values of 0.3, 0.9, 1.5, and 2.2 ± 0.1 × 10^{-11} m^2 s^{-1}, respectively. These results demonstrate the potential to finely control ion transport properties in OIPC systems through thermal treatment of the material.

3.4. Thermal History Effect on Ionic Conductivity in $P_{1222}FSI$. Based on the model developed above one would expect to observe an anisotropy in the macroscopic ion transport within the slowly cooled samples. A preferred orientation direction for the crystallite interfaces should provide a favorable pathway for translational motion, while transport in the other directions would involve more tortuous routes, Figure 7a. Similarly, in the quenched sample the different macroscopic domains present should average out this anisotropy, leaving an isotropic pathway on length scales of ≫1 μm, Figure 7b. Results obtained from AC impedance spectroscopy[43] are consistent with these predictions. Figure 8a,b shows Nyquist plots of impedance data obtained for $P_{1222}FSI$ samples with different thermal histories. The histogram of conductivity values determined with AC electrochemical impedance spectroscopy is displayed in Figure 8c.

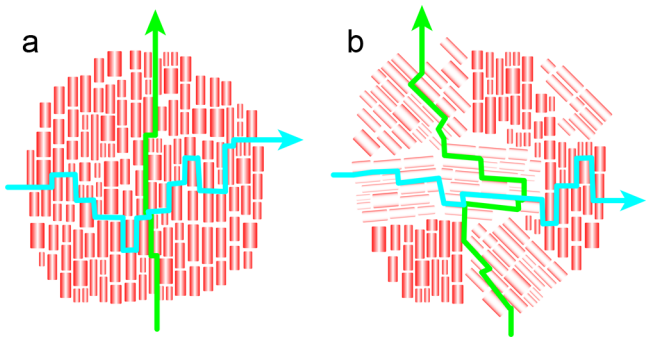

Figure 7. Schematic model of crystallite ordering. (a) Slowly and (b) rapidly cooled $P_{1222}FSI$ samples. The arrows represent example ion conduction pathways through the mobile grain boundary regions when the ions are driven in the vertical (green) or horizontal (blue) directions.

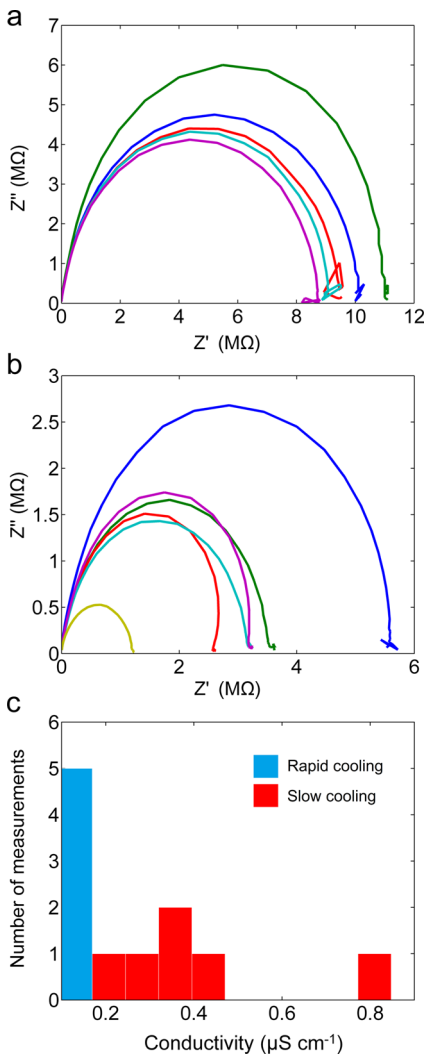

Figure 8. Nyquist plots of impedance data. Nyquist plots obtained for $P_{1222}FSI$ after (a) rapid (1 min) and (b) slow (over 48 h) cooling from the melt (T = 298 K). (c) The histogram of conductivity values determined with AC electrochemical impedance spectroscopy.

Repeated measurements carried out on $P_{1222}FSI$ after melting and rapid cooling gave conductivity values ranging from σ = 1 to 1.2 × 10^{-7} S cm^{-1}. This relatively narrow range reflects the multiple domains of preferred orientation present within the

dx.doi.org/10.1021/ja508290z | J. Am. Chem. Soc. 2014, 136, 15638−15645

sample, which although different in morphology after each quench will give an average effect (global isotropy) over a wide range of length scales. Measurements carried out on the same sample after repeated melting and subsequent slow cooling, however, gave a much broader variation in conductivity (σ = 2 to 9 × 10^{-7} S cm^{-1}). This larger spread reflects the intrinsic conductivity anisotropy arising from a single preferred orientation of grains spanning a large fraction of the sample volume. Exact conductivity values depend on the average orientation of grain boundaries with respect to the applied electric field.

Finally, we note that these alignment-based phenomena are not limited to P_{1222}FSI and appear to be a general feature of plastic crystals due to their polycrystalline nature. We have observed SPRITE T_2* contrast anisotropy in P_{1444}FSI and $P_{1224}PF_6$[8] and also in the nonionic plastic crystal succinonitrile, a molecular plastic crystalline material considered as a universal matrix for solid-state ionic conductors.[44] In the latter system, the T_2* contrast was substantially less pronounced, ≈ 30% at T_P = 1.1 ms (Supporting Information, Figure S3). The T_2* contrast anisotropy observed in succinonitrile can stem from both internal gradients and direct dipolar couplings and will be the subject of future studies.

4. CONCLUSION

Remarkable anisotropic phenomena have been revealed in plastic crystal materials for the first time, using 3D solid-state MRI experiments. The dramatic effect of the cooling rate on diffusion and ionic conductivity of OIPCs is associated with the polycrystalline nature of these materials. One can envisage how the OIPC microstructure could be optimized to result in improved configurations for various electrochemistry applications. This work is therefore expected to impact the performance and design of novel energy storage devices. The SPRITE method has emerged in this study as a powerful tool for the characterization of the internal structure of plastic crystals and potentially a wide range of polycrystalline solids. We believe this to be the first observation of MRI contrast anisotropy due to variations in crystalline domain properties (size and orientation) in a polycrystalline material. This study provides a new insight into the ion transport properties of OIPCs, and it will be followed by a more detailed investigation of the relationship between polycrystalline texture and transport anisotropy, particularly in Li-doped OIPCs that show great promise for use in lithium batteries. Furthermore, we expect the SPRITE method to enable sensitive probing of morphology changes and anisotropic dynamics during *in situ* studies of functioning electrochemical devices, by imaging the electrolyte in these devices during operation.

■ ASSOCIATED CONTENT

Supporting Information

Description of T_2* weighting observed for different T_P's and a reconstructed T_2* map in a rapidly cooled P_{1222}FSI sample, ^{1}H NMR spectra indicating line width anisotropy, T_2* contrast anisotropy observed in nonionic plastic crystal succinonitrile. This material is available free of charge via the Internet at http://pubs.acs.org.

■ AUTHOR INFORMATION

Corresponding Authors

k.romanenko@deakin.edu.au
maria.forsyth@deakin.edu.au

Notes

The authors declare no competing financial interest.

■ ACKNOWLEDGMENTS

The Australian Research Council is acknowledged for funding the Magnetic Resonance Facility through LIEF grant LE11010014 and for funding of the project through the Laureate Fellowship Program FL110100013. Funding through the ARC Centre of Excellence scheme is also gratefully acknowledged.

■ REFERENCES

(1) Taniki, R.; Matsumoto, K.; Hagiwara, R.; Hachiya, K.; Morinaga, T.; Sato, T. *J. Phys. Chem. B* **2013**, *117*, 955.
(2) Abouimrane, A.; Abu-Lebdeb, Y.; Alarco, P. J.; Armand, M. *J. Electrochem. Soc.* **2004**, *151*, A1028.
(3) Abu-Lebdeh, Y.; Abouimrane, A.; Alarco, P. J.; Hammami, A.; Ionescu-Vasii, L.; Armand, M. *Electrochem. Commun.* **2004**, *6*, 432.
(4) Wang, P.; Dai, Q.; Zakeeruddin, S. M.; Forsyth, M.; MacFarlane, D. R.; Gratzel, M. *J. Am. Chem. Soc.* **2004**, *126*, 13590.
(5) Armel, V.; Forsyth, M.; MacFarlane, D. R.; Pringle, J. M. *Energy Environ. Sci.* **2011**, *4*, 2234.
(6) Jin, L. Y.; Howlett, P.; Efthimiadis, J.; Kar, M.; Macfarlane, D. R.; Forsyth, M. *J. Mater. Chem.* **2011**, *21*, 10171.
(7) Sunarso, J.; Shekibi, Y.; Efthimiadis, J.; Jin, L. Y.; Pringle, J. M.; Hollenkamp, A. F.; MacFarlane, D. R.; Forsyth, M.; Howlett, P. C. *J. Solid State Electrochem.* **2012**, *16*, 1841.
(8) Armel, V.; Velayutham, D.; Sun, J.; Howlett, P. C.; Forsyth, M.; MacFarlane, D. R.; Pringle, J. M. *J. Mater. Chem.* **2011**, *21*, 7640.
(9) Jin, L. Y.; Nairn, K. M.; Forsyth, C. M.; Seeber, A. J.; MacFarlane, D. R.; Howlett, P. C.; Forsyth, M.; Pringle, J. M. *J. Am. Chem. Soc.* **2012**, *134*, 9688.
(10) Kidd, B. E.; Lingwood, M. D.; Lee, M.; Gibson, H. W.; Madsen, L. A. *J. Phys. Chem. B* **2014**, *118*, 2176.
(11) Pringle, J. M. *Phys. Chem. Chem. Phys.* **2013**, *15*, 1339.
(12) Michler, G. H. *Electron Microscopy of Polymers*; Springer Verlag: Berlin, 2008.
(13) Key, B.; Bhattacharyya, R.; Morcrette, M.; Seznec, V.; Tarascon, J.-M.; Grey, C. P. *J. Am. Chem. Soc.* **2009**, *131*, 9239.
(14) Bhattacharyya, R.; Key, B.; Chen, H.; Best, A. S.; Hollenkamp, A. F.; Grey, C. P. *Nat. Mater.* **2010**, *9*, 504.
(15) Chandrashekar, S.; Trease, N. M.; Chang, H. J.; Du, L.-S.; Grey, C. P.; Jerschow, A. *Nat. Mater.* **2012**, *11*, 311.
(16) Klett, M.; Giesecke, M.; Nyman, A.; Hallberg, F.; Lindstrom, R. W.; Lindbergh, G.; Furo, I. *J. Am. Chem. Soc.* **2012**, *134*, 14654.
(17) Krachkoyskiy, S. A.; Pauric, A. D.; Halalay, I. C.; Goward, G. R. *J. Phys. Chem. Lett.* **2013**, *4*, 3940.
(18) Ogata, K.; Salager, E.; Kerr, C. J.; Fraser, A. E.; Ducati, C.; Morris, A. J.; Hofmann, S.; Grey, C. P. *Nat. Commun.* **2014**, *5*, 3217.
(19) Callaghan, P. T. *Principles of Nuclear Magnetic Resonance Microscopy*; Oxford University Press: Oxford, 1993.
(20) Price, W. S. *NMR Studies of Translational Motion*; Cambridge University Press: Cambridge, 2009.
(21) Hurlimann, M. D. *J. Magn. Reson.* **1998**, *131*, 232.
(22) Wilson, R. C.; Hurlimann, M. D. *J. Magn. Reson.* **2006**, *183*, 1.
(23) Chen, Q.; Marble, A. E.; Colpitts, B. G.; Balcom, B. J. *J. Magn. Reson.* **2005**, *175*, 300.
(24) Romanenko, K.; Balcom, B. J. *AIChE J.* **2012**, *58*, 3916.
(25) Chavhan, G. B.; Babyn, P. S.; Thomas, B.; Shroff, M. M.; Haacke, E. M. *Radiographics* **2009**, *29*, 1433.
(26) Emid, S.; Creyghton, J. H. N. *Physica B+C (Amsterdam)* **1985**, *128*, 81.
(27) Balcom, B. J.; MacGregor, R. P.; Beyea, S. D.; Green, D. P.; Armstrong, R. L.; Bremner, T. W. *J. Magn. Reson. A* **1996**, *123*, 131.
(28) Mastikhin, I. V.; Balcom, B. J.; Prado, P. J.; Kennedy, C. B. *J. Magn. Reson.* **1999**, *136*, 159.

(29) Beyea, S. D.; Balcom, B. J.; Bremner, T. W.; Prado, P. J.; Green, D. P.; Armstrong, R. L.; Grattan-Bellew, P. E. *Cem. Concr. Res.* **1998**, *28*, 453.
(30) MacMillan, B.; Burke, B.; Balcom, B.; Ziegler, G. *Solid State Nucl. Magn. Reson.* **2005**, *28*, 106.
(31) Ramos-Cabrer, P.; van Duynhoven, J. P. M.; Van der Toorn, A.; Nicolay, K. *Magn. Reson. Imag.* **2004**, *22*, 1097.
(32) Gruwel, M. L. H.; Latta, P.; Tanasiewicz, M.; Volotovskyy, V.; Sramek, M.; Tomanek, B. *Appl. Phys. A: Mater. Sci. Process.* **2007**, *88*, 763.
(33) Weiger, M.; Pruessmann, K. P.; Bracher, A.-K.; Koehler, S.; Lehmann, V.; Wolfram, U.; Hennel, F.; Rasche, V. *NMR Biomed.* **2012**, *25*, 1144.
(34) Tyler, D. J.; Robson, M. D.; Henkelman, R. M.; Young, I. R.; Bydder, G. M. *J. Magn. Reson. Imag.* **2007**, *25*, 279.
(35) Idiyatullin, D.; Corum, C.; Park, J.-Y.; Garwood, M. *J. Magn. Reson.* **2006**, *181*, 342.
(36) McDonald, P. J.; Newling, B. *Rep. Prog. Phys.* **1998**, *61*, 1441.
(37) Cotts, R. M.; Hoch, M. J. R.; Sun, T.; Markert, J. T. *J. Magn. Reson.* **1989**, *83*, 252.
(38) Li, L.; Chen, Q.; Marble, A. E.; Romero-Zeron, L.; Newling, B.; Balcom, B. J. *J. Magn. Reson.* **2009**, *197*, 1.
(39) Oatley, C. W. *Electric and Magnetic Fields: An Introduction*; Cambridge University Press: Cambridge, 1976.
(40) Tanner, J. E. *J. Chem. Phys.* **1970**, *52*, 2523.
(41) Hill, A. J.; Huang, J.; Efthimiadis, J.; Meakin, P.; Forsyth, M.; MacFarlane, D. R. *Solid State Ionics* **2002**, *154*, 119.
(42) Efthimiadis, J.; Forsyth, M.; MacFarlane, D. R. *J. Mater. Sci.* **2003**, *38*, 3293.
(43) Gabrielli, C. *Identification of Electrochemical Processes by Frequency Response Analysis*; The Solartron Electronic Group Ltd.: Farnborough, 1980.
(44) Alarco, P. J.; Abu-Lebdeh, Y.; Abouimrane, A.; Armand, M. *Nat. Mater.* **2004**, *3*, 476.